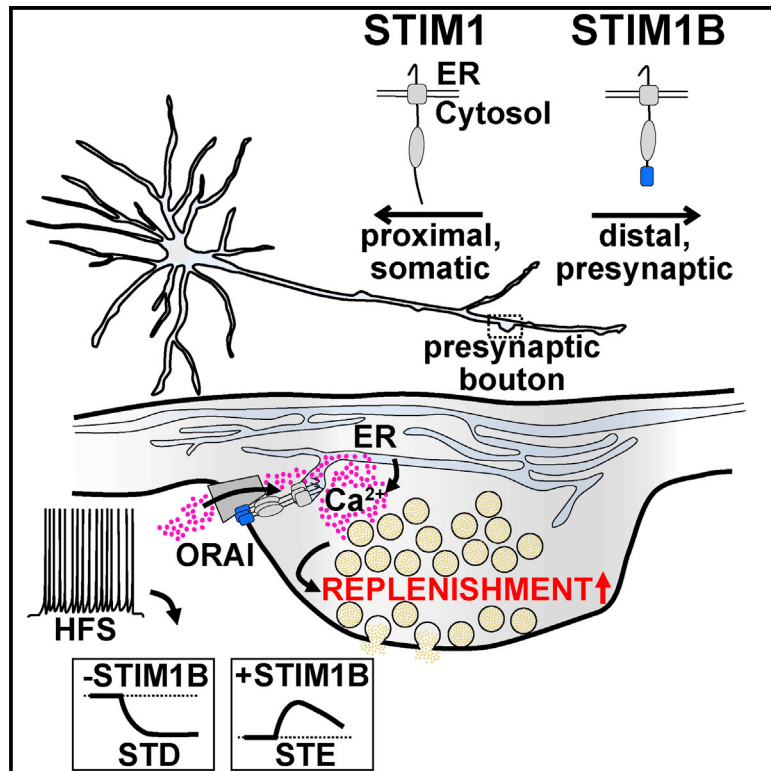


A short isoform of STIM1 confers frequency-dependent synaptic enhancement

Graphical abstract



Authors

Girish Ramesh, Lukas Jarzembowski, Yvonne Schwarz, ..., Dalia Alansary, Dieter Bruns, Barbara A. Niemeyer

Correspondence

barbara.niemeyer@uks.eu

In brief

The role of presynaptic ER in synapse specification is not well known. Ramesh et al. identify an alternative *Stim1* splice variant selectively targeted to presynaptic ER where it converts short-term depression into short-term enhancement (STE) in high-demand situations by increasing recruitment of synaptic vesicles.

Highlights

- STIM1B but not STIM1 localizes to presynaptic ER
- STIM1B causes increased vesicle release at high demand
- STIM1B alters slow Ca²⁺-dependent inactivation of I_{CRAC}
- Splicing alters frequency dependence of synapses and is decreased in AD



Report

A short isoform of STIM1 confers frequency-dependent synaptic enhancement

Girish Ramesh,^{1,5} Lukas Jarzembowski,^{1,5} Yvonne Schwarz,^{2,5} Vanessa Poth,¹ Maik Konrad,¹ Mona L. Knapp,¹ Gertrud Schwär,³ Anna A. Lauer,⁴ Marcus O.W. Grimm,⁴ Dalia Alansary,¹ Dieter Bruns,² and Barbara A. Niemeyer^{1,6,*}

¹Molecular Biophysics, Saarland University, 66421 Homburg, Germany

²Molecular Neurophysiology, Saarland University, 66421 Homburg, Germany

³Biophysics, Center for Integrative Physiology and Molecular Medicine (CIPMM), Bld. 48, Saarland University, 66421 Homburg, Germany

⁴Experimental Neurology, Saarland University, 66421 Homburg, Germany

⁵These authors contributed equally

⁶Lead contact

*Correspondence: barbara.niemeyer@uks.eu

<https://doi.org/10.1016/j.celrep.2021.108844>

SUMMARY

Store-operated Ca^{2+} -entry (SOCE) regulates basal and receptor-triggered Ca^{2+} signaling with STIM proteins sensing the endoplasmic reticulum (ER) Ca^{2+} content and triggering Ca^{2+} entry by gating Orai channels. Although crucial for immune cells, STIM1's role in neuronal Ca^{2+} homeostasis is controversial. Here, we characterize a splice variant, STIM1B, which shows exclusive neuronal expression and protein content surpassing conventional STIM1 in cerebellum and of significant abundance in other brain regions. STIM1B expression results in a truncated protein with slower kinetics of ER-plasma membrane (PM) cluster formation and I_{CRAC} , as well as reduced inactivation. In primary wild-type neurons, STIM1B is targeted by its spliced-in domain B to presynaptic sites where it converts classic synaptic depression into Ca^{2+} - and Orai-dependent short-term synaptic enhancement (STE) at high-frequency stimulation (HFS). In conjunction with altered STIM1 splicing in human Alzheimer disease, our findings highlight STIM1 splicing as an important regulator of neuronal calcium homeostasis and of synaptic plasticity.

INTRODUCTION

Store-operated Ca^{2+} entry (SOCE) links endoplasmic reticulum (ER) Ca^{2+} depletion to reentry from the outside. Depending on the degree of depletion, ER-resident stromal interaction molecules (STIM1/STIM2) are activated, oligomerize, and track to ER and plasma membrane (PM) contact sites where they trap and gate highly Ca^{2+} -selective ORAI channels (reviewed in Prakriya and Lewis, 2015). The thereby generated Ca^{2+} current (I_{CRAC} ; Hoth and Penner, 1992) can be modulated by fast and slow Ca^{2+} -dependent inactivation (FCDI/SCDI) (Zweifach and Lewis, 1995a, 1995b) and is critical for many cellular processes, in particular immune function (reviewed in Feske, 2019). STIM and ORAI genes are ubiquitously expressed, but their roles in the nervous system are less well understood. Recent studies describing neuron-specific deletion of Orai1 and Orai2 channels indicate a role for SOCE in neuronal excitability (Chen-Engerer et al., 2019; Maneshi et al., 2020; Stegner et al., 2019). STIM2 is the predominant paralog in hippocampus and cortex, whereas STIM1 is enriched in the cerebellum (reviewed in Wegierski and Kuznicki, 2018). Forebrain conditional STIM1 knockout mice display significant learning defects (Garcia-Alvarez et al., 2015). In cerebellum, STIM1 maintains a releasable ER Ca^{2+} pool required for postsynaptic dendritic mGluR1 signaling and cerebellar motor behavior (Hartmann et al.,

2014), regulates somatic Ca^{2+} signals and intrinsic spike firing properties (Ryu et al., 2017), and has recently been shown to be critical for intrinsic plasticity of the rapid vestibulo-ocular reflex (VOR) memory (Jang et al., 2020). However, non-canonical functions of STIM1, such as inhibition of L-type voltage-gated Ca^{2+} channels, have also been proposed to influence neuronal excitability (Dittmer et al., 2017; Hawkins et al., 2010; Park et al., 2010). Although these studies address a postsynaptic function of STIM, the role of presynaptic ER is less understood and controversially discussed (Carter et al., 2002; de Juan-Sanz et al., 2017; Emptage et al., 2001; Llano et al., 2000). de Juan-Sanz et al. (2017) detected heterogeneous levels of ER Ca^{2+} in synaptic terminals and postulated that the ER may act as a sink, rather than a source for presynaptic Ca^{2+} . In mouse models of Alzheimer disease (AD), presynaptic Ca^{2+} stores have been shown to control neuronal hyperactivity *in vivo* (Lerdkrai et al., 2018). Here, we identify and characterize a neuron-specific splice variant of STIM1 called STIM1B. Through splice insertion, a targeting motif is added to the cytosolic region of STIM1, allowing for specific localization of STIM1B, but not STIM1, to presynaptic ER. Using a combination of electrophysiological and imaging techniques, we demonstrate that STIM1B slows activation of SOCE and reduces inactivation of I_{CRAC} . Neuronal expression of STIM1B promotes Ca^{2+} -dependent short-term enhancement (STE) of



synaptic signaling at high-frequency stimulation (HFS) due to an increased replenishment rate of synaptic vesicles. Reduced occurrence of STIM1B in AD highlights the pathophysiological relevance of STIM1 splicing. Our results provide insight into the so far poorly understood role of the ER in presynaptic Ca^{2+} homeostasis and suggest that STIM1 splicing can fine-tune synaptic efficacy.

RESULTS

Stim1 exon 11B is a mammalian-specific splice variant expressed in neurons

As an antecedent comment, we will use Stim for murine and STIM for human variants. Both *Stim1* and *Stim2* genes are encoded by large genomic regions spanning ~ 180 kbp and contain 12 exons for the conventional variant; however, database mining predicts multiple splice variants with alternatively inserted exons, requiring an updated exon nomenclature (Figure 1A). The *exon 12* to *exon 14* boundary is a mutually exclusive splice site, which, when splice insertion occurs, results either in insertion of the much longer *exon 13L* (formerly named *exon 11L*, NCBI reference sequence: XM_006507533.4) to translate into a longer Stim1 protein (STIM1L; Darbellay et al., 2011) or in insertion of a short *exon 13B* (NCBI reference sequence: NM_001374060.1). Insertion of *exon 13B* results in a significantly shorter protein lacking 170 amino acids (aa) but contains an added domain of 26 residues based on residues encoded by *exon B* as well as residues due to frame-shifted continuation of translation terminating at E540. Using cDNA derived from different tissues, we screened for *exon B* (13B) versus the known variant ($\emptyset B$) (Figure 1B). Although we did not detect expression of *exon 13B* in cDNA derived from immune cells, astrocytes, testes, lung, skeletal muscle, heart, and kidney ($2^{\Delta\text{Cq}}$ values around 0.003), we found significant expression in the brain ($2^{\Delta\text{Cq}}$ of ~ 1 for cerebellum). Figure 1C shows expression of SOCE genes using calibrated qRT-PCR primers for *Orai1*, *Orai2*, *Orai3*, *Stim1*, and *Stim2* and splice-specific primer sets for *Stim1B* and *Stim1 $\emptyset B$* for different brain regions. As added $2^{-\Delta\text{Cq}}$ values of *Stim1B* and *Stim1 $\emptyset B$* corresponded to the result with *Stim1*-calibrated primers, we assumed equivalent primer efficiencies and calculated the relative expression of *Stim1B* in different brain regions (right column). cDNA isolated from astrocytes or from hippocampal neuronal cultures confirmed neuronal expression of *Stim1B* (Figure S1A). We also investigated *STIM1* splicing in cDNA derived from postmortem brain samples of patients with both familial early onset AD (FAD) or in pooled cDNAs from two cohorts with sporadic AD (14 control [ctrl]/30 AD) and (71 ctrl/145 AD) with age-matched controls (Grimm et al., 2011; Lauer et al., 2020). The relative amount of spliced *STIM1B* was significantly reduced in both familial and sporadic AD (Figure 1D), suggesting aberrant regulation of *STIM1* splicing in AD. Translation of *STIM1B* (Figure 1E) showed domain B downstream of the channel-activation-domain (CAD/SOAR) and of the inhibitory domain (ID). Expression of *Stim1* and *Stim1b* resulted in equal amounts of protein (Figure 1F). Protein amounts in extracts of brain regions were analyzed with an N-terminal epitope antibody recognizing Stim1 at ~ 77 kDa and Stim1B

at expected 62 kDa (Figure 1G), confirming that Stim1B surpasses Stim1 within cerebellum (Figure 1H), which is in good agreement with qRT-PCR results. Evolutionary analysis revealed that *exon B* represents a mammalian splice event with high conservation, although longer variants are also predicted (see # in Figure S1B). We generated a B-specific antibody and subjected cerebellar extracts to immunoprecipitation. Both Stim1 and Stim1B were pulled down with an N-terminal antibody, and predominantly Stim1B was precipitated with the B-specific antibody, whereas a C-term-specific antibody mainly pulled down Stim1 (Figure S1C). Both splice-specific antibodies precipitated little of the other variant, indicating a low degree of dimerization between Stim1 and Stim1B under native conditions. Precipitating Stim2, however, pulled both variants, indicating potentially preferential hetero-dimerization with Stim2 under native conditions (Figure S1D). Using bi-fluorescent complementation assays, we found no difference in the principal ability of STIM1B to interact with STIM1 or STIM2 upon expression in STIM1/2-deficient double knock-out (DKO) HEK cells (HEKDKO; Zhou et al., 2018; Figure S1E).

Stim1B is a differential activator of Orai channels

To understand how splicing affects functionality, we cloned *Stim1/STIM1* and *Stim1B/STIM1B* into bi-cistronic vectors or as *mkate2/YFP*-tagged variants. As the cell line SH-SY5Y also expresses functional VGCC (Sousa et al., 2013), we deleted endogenous *STIM1* and *STIM2* (Figures S1F–S1H) and performed Ca^{2+} imaging experiments after heterologous re-expression. After establishing a baseline, a short high $[\text{K}^+]_o$ -induced depolarizing pulse was applied followed by a SOCE re-addition protocol (Figure 2A). SH-SY5Y *S1/S2*^{-/-} cells showed no SOCE with mock transfection or re-addition of STIM1, or STIM1B did not change basal Ca^{2+} in the presence of endogenous STIM2 (data not shown), but increased basal Ca^{2+} in the DKO background (Figures 2A and 2C). We found little influence of STIM1 or STIM1B on K^+ -induced Ca^{2+} entry. However, STIM1B only partially rescued SOCE and displayed decreased rate, peak, and plateau of SOCE (Figures 2A and 2C), and similar differences in SOCE were recorded with murine variants (see below). We also co-overexpressed STIM1B either with STIM1 or with STIM2 at a 1:1 ratio and found STIM1B to display a dominant-negative phenotype on both STIM1 and STIM2 function (see basal Ca^{2+}) (Figures 2B and 2C). To further investigate biophysical properties of Stim1B versus Stim1, we conducted patch-clamp experiments in co-transfections with different Orai homologs in HEKDKO. Stim1B lead to a decreased rate of I_{CRAC} (Orai1) but reached similar current densities (CDs) within 300 s under conditions of strong intracellular Ca^{2+} buffering (BAPTA+IP₃ in pipette) (Figure 2D). Stim1-induced currents showed $\sim 20\%$ rundown, which may represent slow Ca^{2+} -dependent inactivation (SCDI) versus only $\sim 4\%$ rundown for Stim1B (Figure 2E; % inactivation, see below). Upon co-expression with Orai2, which, together with Orai3, is the prevailing homolog expressed in neurons (Figure 1C), Stim1B showed smaller CDs as well as reduced rundown/SCDI compared to those of Stim1 (Figures 2D and 2E). Co-expression with Orai3 showed an overall faster current onset of I_{CRAC} , with increased

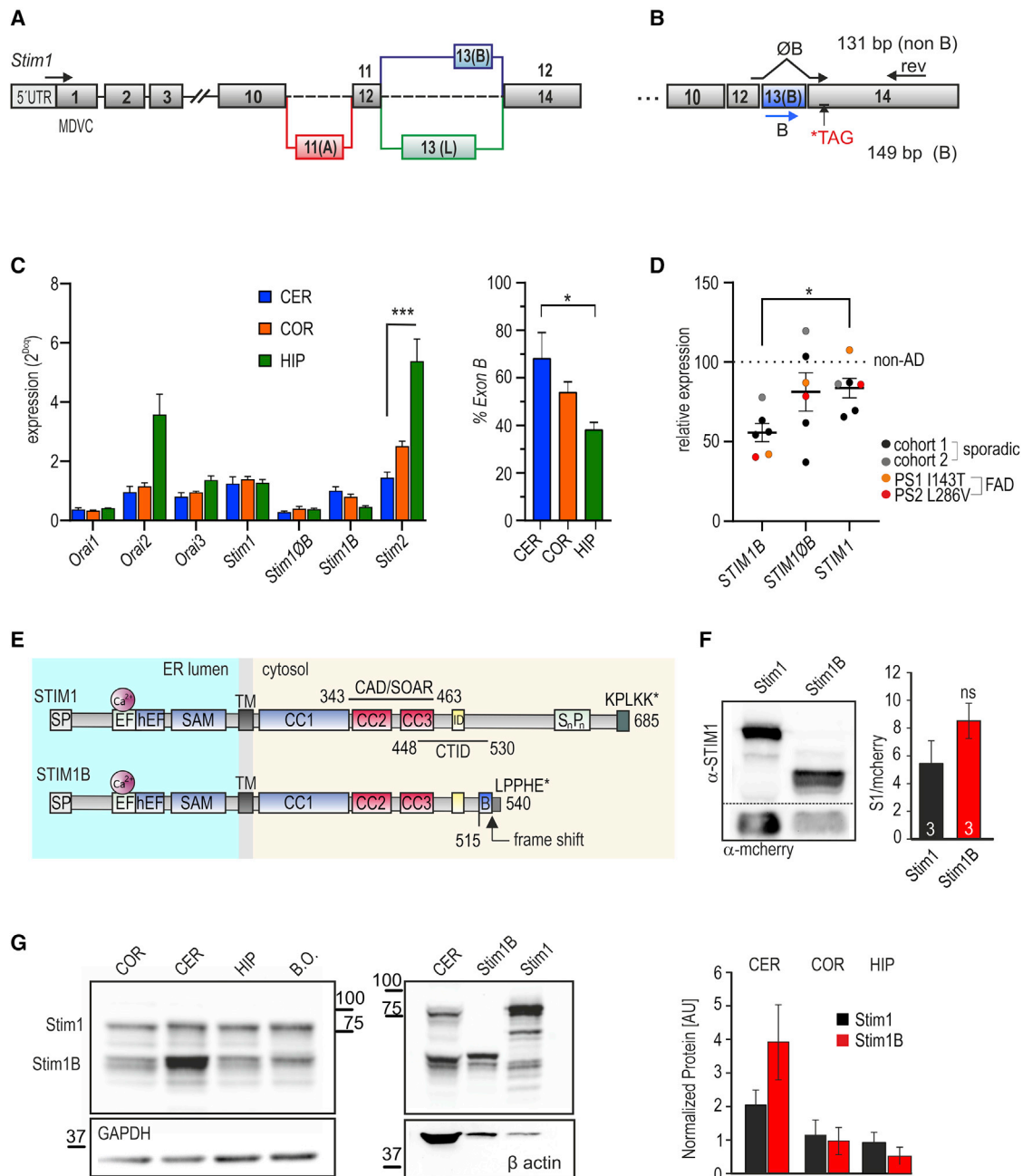


Figure 1. Expression of the *Stim1* exon 13B splice variant

(A) Partial *Stim1* exon structure. Highlighted in red is an alternative exon 11 (A) and the mutually exclusive variants exon 13 (B; blue) and exon 13 (L; green).
 (B) Primer strategy.
 (C) Expression levels normalized to TATA box binding protein (*Tbp*) in brain regions (left) and relative expression of exon B compared to *Stim1* (\pm SD, $n \geq 3$) (right). * $p < 0.05$; one-way ANOVA on ranks followed by Dunn's post-hoc test.
 (D) $2^{-\Delta\Delta C_q}$ values of *STIM1B*, *non-B*, and total *STIM1* of healthy age-matched controls and of familial and sporadic Alzheimer disease patients. * $p < 0.05$; one-way ANOVA on ranks followed by Tukey's post-hoc test.
 (E) Stim and Stim1B protein domains.
 (F) Exemplary western blot of Stim1 and Stim1B using bi-cistronic expression, quantified protein (right).
 (G) Western blot showing Stim1 and Stim1B in different brain regions and heterologous overexpression of Stim1 and Stim1B in HEK293T cells (right). Normalized protein amounts (\pm SD, $n = 3$), detected by an N-terminal Stim1 antibody. See also Figure S1.

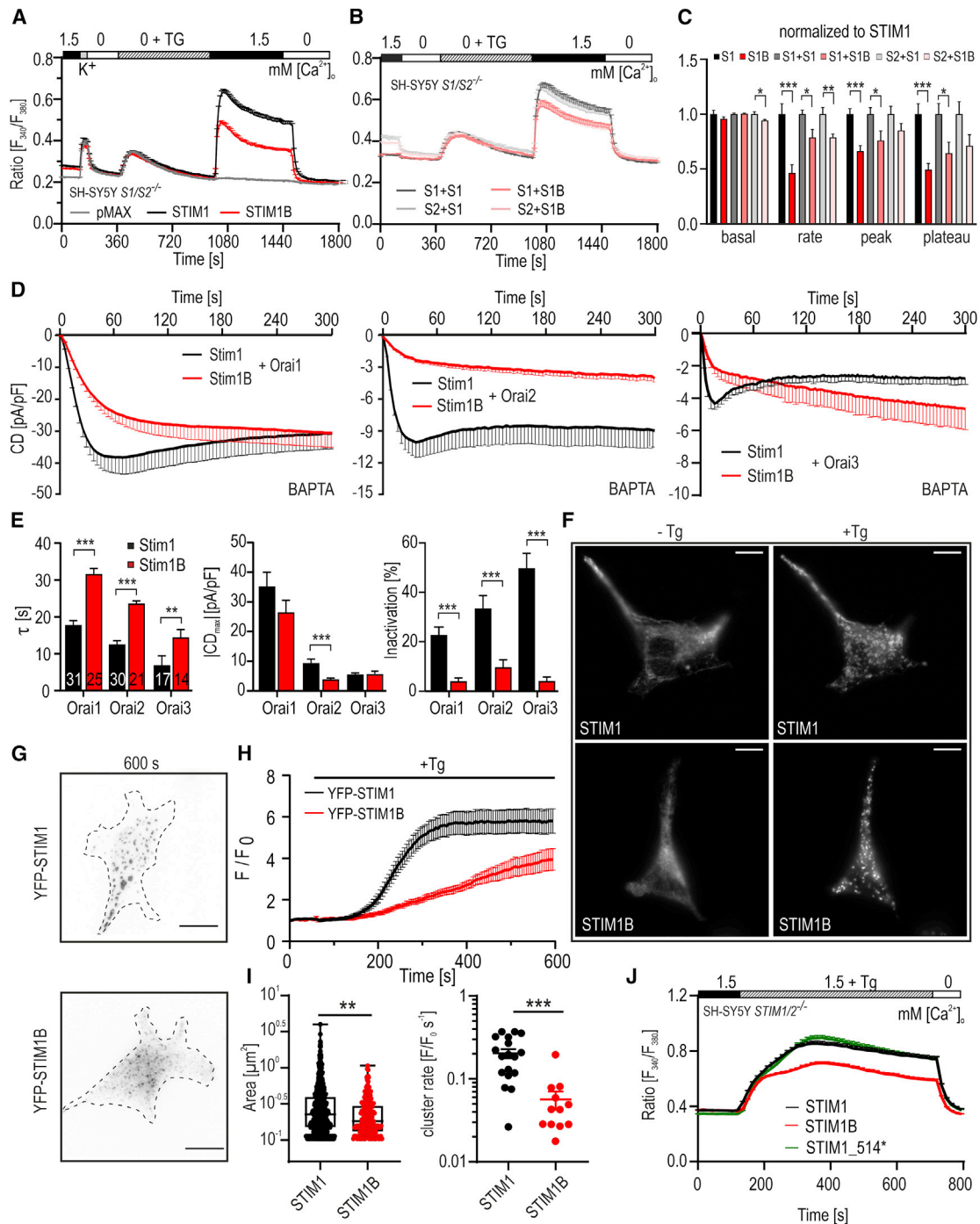


Figure 2. Stim1B is a differential Orai activator with distinct characteristics

(A) SOCE measurements in SH-SY5Y S1/S2^{-/-} with single expression; vector (gray), STIM1 (black), or STIM1B (red) with solution exchanges indicated above.
 (B) SOCE measurements in SH-SY5Y S1/S2^{-/-} with co-overexpression as indicated. S1, STIM1; S2, STIM2.
 (C) Normalized parameters for basal ratio, rate, peak, and plateau of SOCE. All data are presented as mean ± SEM for 6–8 measurements of 3 independent transfections. (n = 150–1,229 cells).
 (D) Whole-cell I_{CRAC} measurements of HEKDKO cells co-expressing Stim1 (black) or Stim1B (red) with either Orai1, Orai2, or Orai3 with 20 mM [BAPTA].
 (E) Quantification of activation kinetics, maximum current density (CD), and inactivation. All data are presented as mean ± SEM (n within first bars).
 (F) Representative widefield images of HEK Orai1^{-/-}; Orai2^{-/-}; Orai3^{-/-} cells expressing YFP-STIM1 or YFP-STIM1B with PLCδ-PH-mCherry (PM marker, not shown) before and after store depletion with Tg. Scale bar, 10 μm.
 (G) Representative TIRF images of HEKDKO expressing YFP-STIM1 or YFP-STIM1B after Tg application; scale bar, 10 μm.

(legend continued on next page)

SCDI/rundown for Stim1 thereby accentuating the difference to Stim1B, which displayed increasing CDs and virtually no SCDI/rundown (Figures 2D and 2E). The finding that τ decreases with Orai2 and Orai3 is expected (Lis et al., 2007), and the similar degree of τ reduction seen with Stim1B argues for an overall similar affinity of Stim1B's CAD domain to Orai isoforms.

STIM1B shows delayed translocation to ER-PM junctions

The C-terminal polybasic domain (PBD) of STIM1 functions as an anchor to attach STIM1 to inner leaflet phospholipids of the PM (Yuan et al., 2009), and the TRIP motif (aa 642–645) is essential to attach STIM1 to the microtubule (MT) tip end binding protein EB1, enabling STIM1 to extend cortical ER structures (Chang et al., 2018; Orci et al., 2009). We investigated targeting and cluster formation of STIM1B lacking these sites in comparison to a deletion mutant terminating after the last common amino acid (STIM1_514*) in cells lacking all endogenous ORAI proteins (Alansary et al., 2020). All three proteins showed ER distribution at rest and cluster formation after thapsigargin (Tg) treatment, with both STIM1_514* and STIM1B resulting in smaller clusters (Figures 2F and S1I). To investigate the kinetics of cluster formation, we applied time-lapse total internal reflection fluorescence (TIRF) microscopy in HEKDKO expressing either YFP-tagged variant. Here, we found that YFP-STIM1 showed initial translocation toward the PM along longitudinal tracks (MTs) (see Video S1), while YFP-STIM1B displayed delayed translocation lacking MT tracking, but eventually formed clusters within the TIRF plane (Figures 2G and 2H; Video S2). The rate and size of clusters are quantified in Figure 2I. Our results show that neither STIM2, the PBD, or the presence of ORAI channels is essential for initial ER-PM cluster formation (see also Zheng et al., 2018) but rather for expansion of cluster sizes. To monitor the onset of SOCE in a similar experimental paradigm, we added Tg in the presence of extracellular Ca^{2+} , resulting in an initial rise in $[\text{Ca}^{2+}]_i$ from the ER, followed by store-operated influx in HEKDKO (Figure 2J). This second phase was delayed for STIM1B, leading to reduced Ca^{2+} influx compared to both STIM1_514* and STIM1 (Figure 2J), indicating that domain B confers an additional phenotype onto STIM1 function.

Insertion of domain B and not the missing C-terminal domain determines the phenotype

The slower activation kinetics observed for Stim1B with all three Orai homologs (Figures 2D and 2E) is congruent with slower cluster formation. Because patch experiments with high BAPTA are not ideal to measure SCDI, we reduced the buffer capacity. To further validate an independent functional role of domain B, we deleted one nucleotide of *Stim1B*'s termination codon to resume the original *Stim1* reading frame (Stim1B \emptyset Stop/Stim1B \emptyset^*),

creating full-length Stim1 with an additional 26 residues (Figure 3A). Stim1/Orai1 I_{CRAC} recorded with 2 mM EGTA showed prominent (~70%) SCDI for Stim1 (Figures 3B and 3C), whereas Stim1B/Orai1 I_{CRAC} displayed significantly reduced I_{CRAC} with slower kinetics and significantly less inactivation (Figures 3B and 3D). Of note, FCDI, recorded by applying voltage pulses to -100 mV, was not significantly affected by Stim1B (Stim1/Orai1 inactivated to $59.48\% \pm 4.7\%$ [SEM] of the peak value and Stim1B/Orai1 to $48.81\% \pm 2.5\%$ of peak value, no significant difference). Our results (Figure 2J) already indicated that Stim1_514* did not phenocopy Stim1B, arguing that the lack of C-terminal residues was not the sole reason for the altered function. Patch-clamp recordings with EGTA showed that Stim1_514* decreased CDs; however, they were significantly larger and more rapidly activating than those of Stim1B. Quite strikingly, Stim1B \emptyset Stop, containing both the MT-tracking EB1 attachment site (TRIP motif) and the PBD, was as slow and inhibited as Stim1B (Figures 3B and 3C), confirming that the B residues confer an independent phenotype. A Stim1B mutant, which contains mutations within the Orai-channel-activating domain (CAD/SOAR), namely, L373S and A376S (CADm), abrogated activation of all Orai channel isoforms (Frischauf et al., 2009) and was unable to evoke currents (Figure 3B). We also recorded these constructs with BAPTA; here, Stim1_514* displayed activation kinetics, CDs, and inactivation comparable to Stim1, whereas Stim1B \emptyset Stop showed slower activation kinetics and less inactivation than Stim1 but slightly faster activation and more inactivation than Stim1B (Figures S2A and S2B). Normalizing BAPTA values to the average EGTA response revealed that current activation kinetics (with IP_3) are Ca^{2+} independent (Figure S2C). However, although maximal CDs of Stim1 were buffer independent, the other variants displayed significant increases. As expected, SCDI is strongly reduced in BAPTA for all constructs and virtually absent in Stim1B (Figure S2C). Ca^{2+} imaging confirmed phenotypes for N-terminally tagged constructs (Figure S2D) used for expression in neurons. These results clearly indicate that insertion of domain B and not deletion of C-terminal residues confers specific changes.

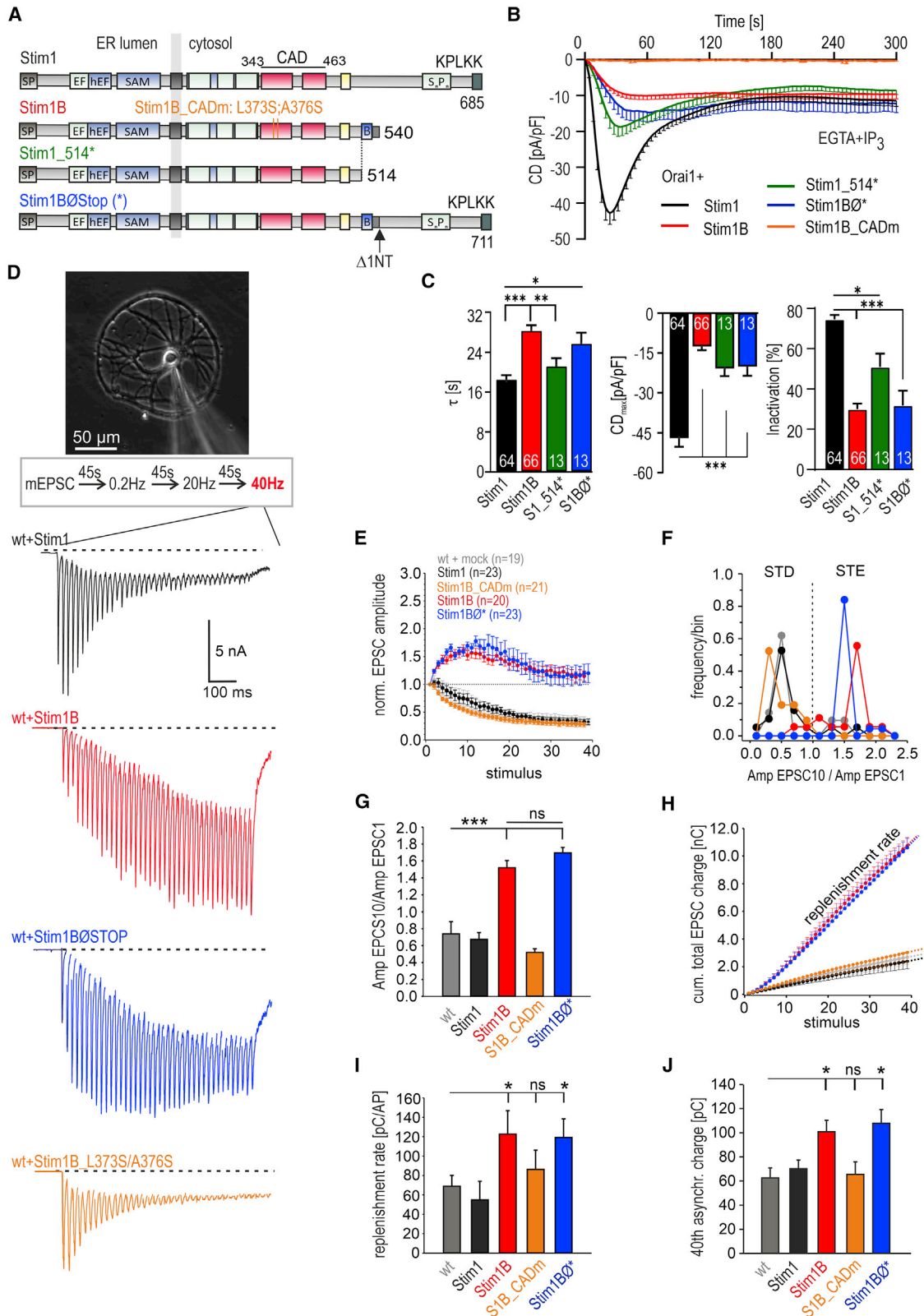
Stim1B but not of Stim1 turns synaptic depression into short-term enhancement

Given the exclusive neuronal expression of *Stim1B* (see Figure 1; Figure S1A), we investigated whether Stim1 or Stim1B differentially affects synaptic transmission. Stim1, Stim1B, and mutant variants were virally transduced in autaptic hippocampal cultures. To cover a range of synaptic responses, we first recorded spontaneous activity, followed by a 0.2-Hz stimulus and subsequent 20-Hz and 40-Hz HFS trains (Figure 3D). Expression of Stim1 or Stim1B did not alter miniature excitatory postsynaptic current (mEPSC) signaling, neither changing frequency, amplitude, or charge of spontaneous neurotransmitter

(H) F/F₀ over time of YFP-STIM1 (black) or YFP-STIM1B (red) monitored by TIRF microscopy.

(I) Quantification of cluster size and rate of formation. Intensity change and cluster rate are presented as mean \pm SEM and cluster size as boxplot (229–923 clusters, median with 25th–75th percentile, whiskers represent min. and max. values). All data were obtained from 12–18 cells with 2–5 technical and 5 biological replicates each. Significance for all statistics is represented as follows: * $p < 0.05$, ** $p < 0.01$, *** $p < 0.001$; one-way ANOVA on ranks followed by Dunn's post hoc test.

See also Figures S1 and S2.



(legend on next page)

release (Figures S2E–S2G). Also, kinetics of single quantal events remained unchanged (data not shown), indicating that Stim1 or Stim1B did not influence the postsynaptic receptor machinery. Furthermore, we found no alteration in basal action-potential-evoked release (stimulation frequency, 0.2 Hz) (Figure S2H). To investigate potential effects of Stim1B expression on synaptic efficacy, we used 20-Hz HFSs (Figure S3) and found that neither variant altered the initial EPSC amplitude (Figure S3D), nor affected the time course of synaptic depletion or vesicle pool size (Figures S3A–S3G). Surprisingly, subsequent 40-Hz HFS activation uncovered a strong Stim1B phenotype, with Stim1-expressing neurons showing classic short-term depression (STD) indistinguishable from mock-transduced neurons (Figures 3D–3G). In contrast, starting from a similar initial amplitude, Stim1B caused strong short-term enhancement (STE) over the stimulus train (Figures 3D–3G). Furthermore, the AmpEPSC10/AmpEPSC1 ratio was shifted toward higher values (Figure 3F), reaching on average a nearly 1.5-fold higher ratio than in mock-transfected or Stim1-expressing neurons (Stim1B-positive neurons: 1.52 ± 0.084 ; Stim1 expressing neurons: 0.67 ± 0.082 ; $p < 0.001$, one-way ANOVA on ranks; Figure 3F). Moreover, the total charge transfer of the evoked response (Figure 3H) and the replenishment rate (slope of the cumulative total charge for the last four stimuli; Schwarz et al., 2019) were strongly enhanced in Stim1B-positive cells compared with that of Stim1-expressing neurons. Along the same line, the asynchronous release was increased upon Stim1B expression (Figure 3J), indicating enhanced Ca^{2+} levels in the presynaptic terminal. This strong synaptic phenotype was also observed upon expression of Stim1B Δ Stop, producing a profound STE of synaptic signaling that was indistinguishable from Stim1B (Figure 3). These results are consistent with the phenotypic similarities in heterologous expression and indicate a role of domain B and not the lack of C-terminal Stim1 residues in synaptic plasticity. In contrast, the Stim1B CAD mutant failed to evoke STE and displayed a synaptic phenotype similar to non-transduced or Stim1-transduced neurons, even displaying a tendency toward an enhanced rate of synaptic depression (Figures 3D–3F). The failure of Stim1B_CADm to support STE suggests that presynaptic Ca^{2+} influx through Orai channels directly or indirectly (by filling the ER) mediates Stim1B's effect on STE. Taken together, these results suggest a role for Stim1B in modulating synaptic efficiency. To validate that STE is indeed dependent on an increase in presynaptic Ca^{2+} , we used EGTA-acetoxymethyl ester (AM) to buffer the intracellular Ca^{2+} rise

during HFS (Otsu et al., 2004). EGTA-AM treatment fully abolished Stim1B-mediated STE (Figures S3H–S3L). The AmpEPSC10/AmpEPSC1 ratio was shifted toward STD for all measured groups (Figure S3J). Conversely, the elevated asynchronous release component during HFS reporting the accumulation of intra-terminal Ca^{2+} (Otsu et al., 2004) was completely abolished with EGTA-AM treatment, indicating efficient Ca^{2+} buffering (Figures S3K and S3L). We thus raised the question whether the phenotype observed at 40 Hz was truly frequency dependent or whether STE was due to an accumulation of presynaptic $[Ca^{2+}]$ triggered by the preceding 20-Hz train. For this question, we recorded a second 20-Hz train with the same inter-stimulus interval as before (Figure S4A). Indeed, both Stim1B and Stim1B Δ Stop now caused STE at the second 20-Hz train, which was absent in the other groups (Figures S4A–S4F), and the initial amplitude remained unchanged among the different groups (Figure S4D). Overall, the phenotypical similarities of Stim1B expression recorded at different stimulation frequencies point toward a mechanism in which a rise in presynaptic $[Ca^{2+}]$ is required to trigger Stim1B-mediated STE. The comparative analyses of Stim1B and its mutant variants indicate a crucial role of Stim1 domain B in regulating synaptic STE, which could be mediated either by additional Ca^{2+} influx or by ER Ca^{2+} release directly or indirectly through activation of synaptic Orai channels.

Presynaptic localization corroborates synaptic physiology of Stim1B

Given the strong synaptic phenotype described above, we investigated protein localization in hippocampal mass cultures. Stim1 localized mainly to the ER within the neuronal soma with some fluorescence protruding into the larger dendritic or axonal structures and displayed little co-localization with the presynaptic marker protein bassoon (Figures 4A and 4B). Stim1B, however, showed a clearly distinct localization with some somatic ER localization (not seen in Figure 4A) but a much more distal punctate localization that significantly overlapped with the presynaptic marker bassoon (Figures 4A and 4B). To investigate whether the differential localization is due to the absence of C-terminal residues and binding partners, we tested Stim1B Δ Stop. Stim1B Δ Stop still maintained the differential localization compared to Stim1 and displayed co-localization with bassoon (Figures 4A and 4B), confirming that specific residues are necessary for localization and that the STE phenotype is due to presynaptically localized Stim1B. Similarly, the ORAI-coupling-deficient Stim1B_L373S;A376S

Figure 3. Domain B dictates phenotype and promotes strong STE of synaptic signaling

- (A) Schematic representation of Stim1, Stim1B, and derived mutant proteins.
 (B) Average traces showing CD over time in cells with indicated Stim1 variant co-expressed with Orai1 (2 mM EGTA).
 (C) Quantification of patch-clamp data in (B) showing mean \pm SEM of fitted activation kinetics, maximal CDs (CD_{max}) and % inactivation (n within bars).
 (D) Exemplary image of a patch-clamped autaptic neuron with stimulation protocol and sample recordings of action potential (AP)-evoked EPSCs (excitatory postsynaptic currents; 40 Hz) shown below.
 (E) EPSC amplitude changes during HFS normalized to the initial amplitude.
 (F and G) Frequency distribution of AmpEPSC10/AmpEPSC1 ratio shows that Stim1B expression shifts synaptic responses toward STE.
 (H) Mean cumulative total charge transfer during HFS. The replenishment rate was determined from the slope of the cumulative plot (last 4 data points).
 (I) The replenishment rate is significantly enhanced in Stim1B- or Stim1B Δ Stop-expressing neurons compared with that of the other groups.
 (J) Quantification of the 40th asynchronous charge. Data were collected from 3–4 independent preparations; * $p < 0.05$, ** $p < 0.01$, *** $p < 0.001$; one-way ANOVA on ranks followed by Dunn's post hoc test.

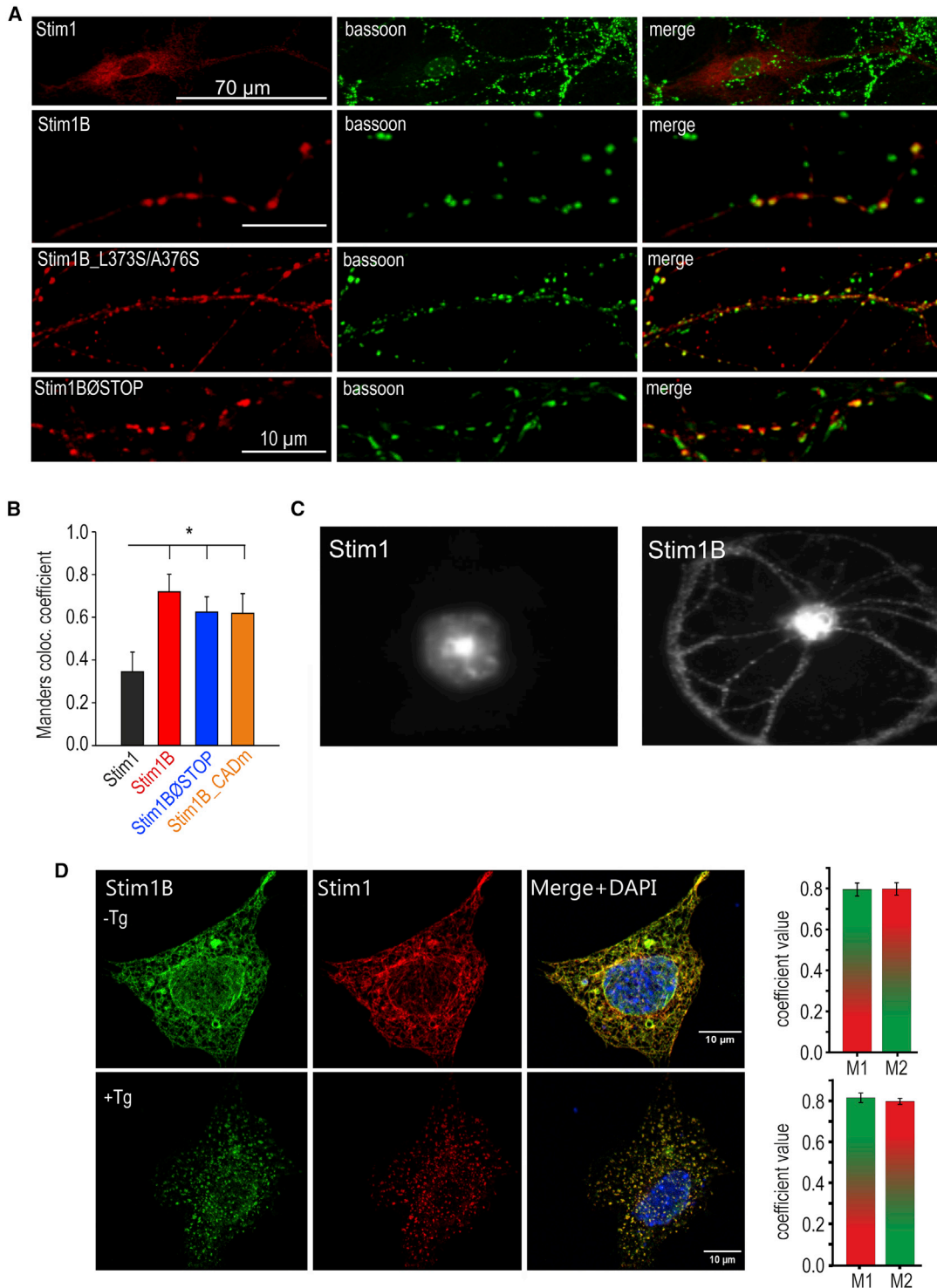


Figure 4. Stim1B is localized to presynaptic terminals

(A) Representative images of variants (left) co-immunolabeled with an anti-mkate2 antibody and presynaptic bassoon (middle).

(B) Quantification of colocalization in thin axonal structures. 12 Stim1-, 8 Stim1B-, 6 Stim1B_CADm-, and 7 Stim1BØStop-expressing neurons from 2 independent cultures were analyzed. $p < 0.05$; one way ANOVA on ranks/Dunn's post hoc test.

(C) Exemplary *in vivo* fluorescence of mkate2-Stim1- and mkate2-Stim1B-expressing neurons.

(D) Confocal images of MEF cells co-expressing Stim1B and Stim1. A monoclonal C-terminal antibody detected Stim1, whereas the B-specific antibody detected Stim1B. Co-localization was quantified using Manders' coefficients.

still localized to presynaptic sites (Figures 4A and 4B), proving that its absent STE (Figures 3 and S4) was not due to altered localization. The extent of stronger peripheral localization of Stim1B can also be directly visualized with live microscopy visualizing mKate2 fluorescence of patch-clamped neurons (Figure 4C). In contrast to the differential localization of Stim1B versus Stim1 observed in neurons, co-expression of both proteins in mouse embryonic fibroblasts (MEFs) displayed a high degree of co-localization within the ER before or after Tg treatment (Figure 4D). In summary, the distinct localization of Stim1B to presynaptic terminals together with its enhancement of synaptic responsiveness at HFS adds evidence for SOCE dynamically shaping STE in high-demand situations.

DISCUSSION

The human genome consists of ~20,600 protein-coding genes, which is surprisingly low for the proteomic complexity in tissues, but with an average of 6.3 alternatively spliced transcripts (3.9 different protein-coding transcripts) per locus (The ENCODE Project Consortium, 2012). Of several predicted *Stim1* splice variants, *Stim1B* is highly enriched in the CNS, suggesting a selective advantage correlated with mammalian brain function (Figure S1). Although abundant in several brain regions, *exon B* and the corresponding Stim1B protein is the dominant Stim1 isoform in cerebellum, while still contributing to ~40% of Stim1 protein in hippocampus. In postmortem brain samples of age-matched controls or patients with early onset or sporadic AD, *STIM1B* is detected and shows a decreased expression in AD compared to *STIM1*, indicating altered splicing in AD. Functionally, Stim1B displayed several distinct features, as follows: in heterologous expression systems, Stim1B lead to slower recruitment toward ER-PM junctional regions, smaller puncta, and slower activation of all Orai isoforms, also in the presence of STIM2 (Figure 2). These effects are small in patch-clamp experiments with overexpression of Orai1 and with strong buffering, indicating the near-normal interaction and gating of Orai1, which was also confirmed by unaltered fast inactivation (FCDI). As also described by Zheng et al. (2018), larger C-terminal deletions in STIM1 obliterate the attachment to MTs by EB1 proteins, the detachment from which is facilitated by the PBD (Chang et al., 2018) and explains that deletion of only the PBD (ΔK) may be less active than larger deletions. In addition, SCDI was significantly reduced with Stim1B, which may be due to slower store refilling, altered phosphorylation (Zweifach and Lewis, 1995b), decreased disassembly, and/or altered interaction with SARAF (Palty et al., 2012) or with unknown proteins. In co-expression with Orai3, Stim1B resulted in a continuous run-up of I_{CRAC} in contrast to the rundown seen with co-expression of Stim1. The slowed I_{CRAC} and SOCE activation kinetics and reduced peak response were not well phenocopied by the artificially deleted Stim1_514* but instead recapitulated with insertion of the specific and conserved residues into full-length Stim1 (Stim1B Δ Stop), arguing for an added function conferred by the specific residues. This added function is critical for targeting Stim1B to presynaptic sites, where expression of Stim1B but not of Stim1 switched synaptic transmission at HFS

(40 Hz), from STD to short-term facilitation of synaptic signaling by increasing vesicle replenishment rate. This strong enhancement was also observed with Stim1B Δ Stop but not with Stim1B_CADm. Potentially, Stim1B might recruit endogenous full-length Stim1 or Stim2 to presynaptic ER; however, we found little evidence for Stim1 and Stim1B interaction in co-immunoprecipitation from cerebellar extracts. Stim2 was able to interact with both variants; however, the functional roles of Stim2 in presynaptic regions have not been described. Buffering Ca^{2+} abolished Stim1B-mediated STE, suggesting that STE is caused by an increase in cytosolic Ca^{2+} , which is also supported by the fact that a second 20-Hz stimulus displayed STE in the presence of Stim1B. Thus, Ca^{2+} influx through voltage-gated Ca^{2+} channels (VGCC) (during the initial stimulus train) and subsequent increase in $[Ca^{2+}]_i$ are prerequisites for Stim1B-mediated STE of synaptic signaling. In contrast to the reported inhibition of postsynaptic VGCC by Stim1 (Dittmer et al., 2017), a direct inhibition of presynaptic VGCC by Stim1B is unlikely, given that we did not observe changes in the initial EPSC amplitude and RRP size, with both parameters being reduced in the case of VGCC inhibition (Catterall and Few, 2008). The increase in replenishment rate, as well as in asynchronous release observed with Stim1B (Figures 3 and S4), points to a mechanism whereby presynaptic localized Stim1B functionally couples to Orai channels, providing an additional Ca^{2+} entry pathway (into cytosol/ER) required for vesicle replenishment and/or recruitment during protracted stimulation. Indeed, the L373S;A376S mutation within the CAD domain of Stim1B completely abrogated STE (Figures 3B and 3F–3J), pointing to a bona fide role for Stim1B-mediated SOCE in being able to support or trigger STE at high frequencies. The slower time course of I_{CRAC} activation in heterologous expression compared to that of EPSCs measured in Figure 3 suggests that in neurons, Stim1B is likely pre-coupled to Orai channels at specified presynaptic contact sites (as postulated by Maneshi et al., 2020 for Orai1 in dendritic spines) or that slower Stim1B-mediated SOCE is sufficient to keep ER stores charged to provide local HFS-induced Ca^{2+} -induced Ca^{2+} release (CICR). Voltage-gated Ca^{2+} entry (VGCE) at the active zone can rapidly trigger further Ca^{2+} influx across the PM through other Ca^{2+} -activated channels (i.e., TRPC1/C5; Schwarz et al., 2019), which could enhance CICR and induce SOCE to mobilize more distantly localized synaptic vesicles in order to maintain STE of synaptic signaling. Given that basal transmission was unaltered by Stim1B expression suggests that Stim1B is selectively engaged to support vesicle replenishment in high-demand situations. Although frequency-dependent changes in synaptic strength are important for gain control and sensory adaptation (Abbott and Regehr, 2004), vestibular and Purkinje cell to deep cerebellar nuclear (PC to DCN) inhibitory synapses are frequency invariant, with Synaptotagmin-7, the Ca^{2+} sensor for STE, supporting facilitation at increasing firing frequencies to counteract depression (Turecek et al., 2017). In summary, our data imply that the neuronal splice variant Stim1B is selectively targeted to presynaptic ER to trigger an additional Ca^{2+} influx pathway to replenish synaptic vesicles from a reserve pool. Therefore, the relative amount of spliced Stim1 in different neurons and potentially in different synapses of the same

neuron may provide an elegant mechanism enabling synapses to tune their synaptic efficacy. This adaptation appears reduced in neurodegenerative diseases such as AD with significantly reduced *STIM1B* splicing.

STAR★METHODS

Detailed methods are provided in the online version of this paper and include the following:

- **KEY RESOURCES TABLE**
- **RESOURCE AVAILABILITY**
 - Lead contact
 - Materials availability
 - Data and code availability
- **EXPERIMENTAL MODEL AND SUBJECT DETAILS**
 - Animals
 - Cell culture of cell lines
 - Primary hippocampal neuron cultures
 - Generation of CRISPR-Cas9-mediated STIM1/STIM2 knockout cell lines
- **METHOD DETAILS**
 - Plasmids and cloning
 - Transfection
 - PCR and quantitative real-time PCR
 - Biochemistry
 - Electrophysiological measurements of I_{CRAC}
 - Recordings of autaptic synaptic currents
 - TIRF and widefield microscopy of cluster formation
 - Fura2-based Ca^{2+} Imaging
 - Bimolecular fluorescence complementation
 - Immunostaining
- **QUANTIFICATION AND STATISTICAL ANALYSIS**
 - Quantification of colocalization
 - Quantification of TIRF microscopy data
 - Statistical analysis

SUPPLEMENTAL INFORMATION

Supplemental information can be found online at <https://doi.org/10.1016/j.celrep.2021.108844>.

ACKNOWLEDGMENTS

We thank Drs. E. Krause and M. Jung for help with the LSM microscope and for generation of the Stim1B antibody, K. Förderer for technical help, and C. Hoxha and S. Janku for cell culture work. We thank A. Gilson and Dr. A. Lis for initial PCR experiments and members of the Hoth, Niemeyer, and Bruns labs for critical input, reading of the manuscript, and discussions. This work was supported by the Deutsche Forschungsgemeinschaft (DFG): CRC1027 (C4/C7), CRC894 (A2), and TRR219 (C-09) to B.A.N.; IRTG 1830 to M.L.K.; CRC1027 (C5) to D.B.; and UdS funding (HOMFOR) to Y.S.

AUTHOR CONTRIBUTIONS

G.R. performed patch-clamp experiments, immune precipitations, cloning, and western blots; L.J., M.K., and V.P. performed imaging, cloning, and immunohistochemistry; Y.S. prepared neuronal cultures and conducted patch-clamp and immunohistochemistry of neurons; D.A. contributed to cloning, imaging, and patch-clamp experiments; M.L.K. conducted BIFC experiments; G.S. conducted qRT-PCR experiments; and A.A.L. and M.O.W.G. initiated

SH-SY5Y CRISPR-Cas9-modified cells with further help by M.K. and V.P. and provided qRT-PCR analysis of AD patients. All authors conducted data analysis. B.A.N., Y.S., and D.B. designed experiments and B.A.N. wrote the manuscript with input by all authors.

DECLARATION OF INTERESTS

The authors declare no competing interests.

Received: September 3, 2020

Revised: December 16, 2020

Accepted: February 17, 2021

Published: March 16, 2021

REFERENCES

- Abbott, L.F., and Regehr, W.G. (2004). Synaptic computation. *Nature* *431*, 796–803.
- Alansary, D., Peckys, D.B., Niemeyer, B.A., and de Jonge, N. (2020). Detecting single ORAI1 proteins within the plasma membrane reveals higher-order channel complexes. *J. Cell Sci.* *133*, jcs240358.
- Carter, A.G., Vogt, K.E., Foster, K.A., and Regehr, W.G. (2002). Assessing the role of calcium-induced calcium release in short-term presynaptic plasticity at excitatory central synapses. *J. Neurosci.* *22*, 21–28.
- Catterall, W.A., and Few, A.P. (2008). Calcium channel regulation and presynaptic plasticity. *Neuron* *59*, 882–901.
- Chang, C.L., Chen, Y.J., Quintanilla, C.G., Hsieh, T.S., and Liou, J. (2018). EB1 binding restricts STIM1 translocation to ER-PM junctions and regulates store-operated Ca^{2+} entry. *J. Cell Biol.* *217*, 2047–2058.
- Chen-Engerer, H.J., Hartmann, J., Karl, R.M., Yang, J., Feske, S., and Konnerth, A. (2019). Two types of functionally distinct Ca^{2+} stores in hippocampal neurons. *Nat. Commun.* *10*, 3223.
- Darbellay, B., Amaudeau, S., Bader, C.R., König, S., and Bernheim, L. (2011). STIM1L is a new actin-binding splice variant involved in fast repetitive Ca^{2+} release. *J. Cell Biol.* *194*, 335–346.
- de Juan-Sanz, J., Holt, G.T., Schreiter, E.R., de Juan, F., Kim, D.S., and Ryan, T.A. (2017). Axonal Endoplasmic Reticulum Ca^{2+} Content Controls Release Probability in CNS Nerve Terminals. *Neuron* *93*, 867–881.e6.
- Dittmer, P.J., Wild, A.R., Dell'Acqua, M.L., and Sather, W.A. (2017). STIM1 Ca^{2+} Sensor Control of L-type Ca^{2+} -Channel-Dependent Dendritic Spine Structural Plasticity and Nuclear Signaling. *Cell Rep.* *19*, 321–334.
- Emptage, N.J., Reid, C.A., and Fine, A. (2001). Calcium stores in hippocampal synaptic boutons mediate short-term plasticity, store-operated Ca^{2+} entry, and spontaneous transmitter release. *Neuron* *29*, 197–208.
- Feske, S. (2019). CRAC channels and disease - From human CRAC channelopathies and animal models to novel drugs. *Cell Calcium* *80*, 112–116.
- Frischauf, I., Muik, M., Derler, I., Bergsmann, J., Fahrner, M., Schindl, R., Groschner, K., and Romanin, C. (2009). Molecular determinants of the coupling between STIM1 and Orai channels: differential activation of Orai1-3 channels by a STIM1 coiled-coil mutant. *J. Biol. Chem.* *284*, 21696–21706.
- García-Alvarez, G., Shetty, M.S., Lu, B., Yap, K.A., Oh-Hora, M., Sajikumar, S., Bichler, Z., and Fivaz, M. (2015). Impaired spatial memory and enhanced long-term potentiation in mice with forebrain-specific ablation of the Stim genes. *Front. Behav. Neurosci.* *9*, 180.
- Grimm, M.O., Grösgen, S., Riemenschneider, M., Tanila, H., Grimm, H.S., and Hartmann, T. (2011). From brain to food: analysis of phosphatidylcholins, lysophosphatidylcholins and phosphatidylcholin-plasmalogens derivatives in Alzheimer's disease human post mortem brains and mice model via mass spectrometry. *J. Chromatogr. A* *1218*, 7713–7722.
- Hartmann, J., Karl, R.M., Alexander, R.P., Adelsberger, H., Brill, M.S., Rühlmann, C., Ansel, A., Sakimura, K., Baba, Y., Kurosaki, T., et al. (2014). STIM1 controls neuronal Ca^{2+} signaling, mGluR1-dependent synaptic transmission, and cerebellar motor behavior. *Neuron* *82*, 635–644.

- Hawkins, B.J., Irrinki, K.M., Mallilankaraman, K., Lien, Y.C., Wang, Y., Bhanumathy, C.D., Subbiah, R., Ritchie, M.F., Soboloff, J., Baba, Y., et al. (2010). S-glutathionylation activates STIM1 and alters mitochondrial homeostasis. *J. Cell Biol.* **190**, 391–405.
- Hoth, M., and Penner, R. (1992). Depletion of intracellular calcium stores activates a calcium current in mast cells. *Nature* **355**, 353–356.
- Jang, D.C., Shim, H.G., and Kim, S.J. (2020). Intrinsic plasticity of cerebellar Purkinje cells contributes to motor memory consolidation. *J. Neurosci.* **40**, 4145–4157.
- Jing, J., He, L., Sun, A., Quintana, A., Ding, Y., Ma, G., Tan, P., Liang, X., Zheng, X., Chen, L., et al. (2015). Proteomic mapping of ER-PM junctions identifies STIMATE as a regulator of Ca²⁺ influx. *Nat. Cell Biol.* **17**, 1339–1347.
- Kilch, T., Alansary, D., Peglow, M., Dörr, K., Rychkov, G., Rieger, H., Peinelt, C., and Niemeyer, B.A. (2013). Mutations of the Ca²⁺-sensing stromal interaction molecule STIM1 regulate Ca²⁺ influx by altered oligomerization of STIM1 and by destabilization of the Ca²⁺ channel Orai1. *J. Biol. Chem.* **288**, 1653–1664.
- Lauer, A.A., Mett, J., Janitschke, D., Thiel, A., Stahlmann, C.P., Bachmann, C.M., Ritzmann, F., Schrul, B., Müller, U.C., Stein, R., et al. (2020). Regulatory feedback cycle of the insulin-degrading enzyme and the amyloid precursor protein intracellular domain: Implications for Alzheimer's disease. *Aging Cell* **19**, e13264.
- Lerdkrai, C., Asavapanumas, N., Brawek, B., Kovalchuk, Y., Mojtahedi, N., Olmedillas Del Moral, M., and Garaschuk, O. (2018). Intracellular Ca²⁺ stores control in vivo neuronal hyperactivity in a mouse model of Alzheimer's disease. *Proc. Natl. Acad. Sci. USA* **115**, E1279–E1288.
- Liou, J., Kim, M.L., Heo, W.D., Jones, J.T., Myers, J.W., Ferrell, J.E., Jr., and Meyer, T. (2005). STIM is a Ca²⁺ sensor essential for Ca²⁺-store-depletion-triggered Ca²⁺ influx. *Curr. Biol.* **15**, 1235–1241.
- Lis, A., Peinelt, C., Beck, A., Parvez, S., Monteilh-Zoller, M., Fleig, A., and Penner, R. (2007). CRACM1, CRACM2, and CRACM3 are store-operated Ca²⁺ channels with distinct functional properties. *Curr. Biol.* **17**, 794–800.
- Llano, I., González, J., Caputo, C., Lai, F.A., Blayney, L.M., Tan, Y.P., and Marty, A. (2000). Presynaptic calcium stores underlie large-amplitude miniature IPSCs and spontaneous calcium transients. *Nat. Neurosci.* **3**, 1256–1265.
- Maneshi, M.M., Toth, A.B., Ishii, T., Hori, K., Tsujikawa, S., Shum, A.K., Shrestha, N., Yamashita, M., Miller, R.J., Radulovic, J., et al. (2020). Orai1 Channels Are Essential for Amplification of Glutamate-Evoked Ca²⁺ Signals in Dendritic Spines to Regulate Working and Associative Memory. *Cell Rep.* **33**, 108464.
- Oh-Hora, M., Yamashita, M., Hogan, P.G., Sharma, S., Lamperti, E., Chung, W., Prakriya, M., Feske, S., and Rao, A. (2008). Dual functions for the endoplasmic reticulum calcium sensors STIM1 and STIM2 in T cell activation and tolerance. *Nat. Immunol.* **9**, 432–443.
- Orci, L., Ravazzola, M., Le Coadic, M., Shen, W.W., Demaurex, N., and Cosson, P. (2009). From the Cover: STIM1-induced precortical and cortical subdomains of the endoplasmic reticulum. *Proc. Natl. Acad. Sci. USA* **106**, 19358–19362.
- Otsu, Y., Shahrezaei, V., Li, B., Raymond, L.A., Delaney, K.R., and Murphy, T.H. (2004). Competition between phasic and asynchronous release for recovered synaptic vesicles at developing hippocampal autaptic synapses. *J. Neurosci.* **24**, 420–433. <https://doi.org/10.1523/JNEUROSCI.4452-03.2004>.
- Palty, R., Raveh, A., Kaminsky, I., Meller, R., and Reuveny, E. (2012). SARAF inactivates the store operated calcium entry machinery to prevent excess calcium refilling. *Cell* **149**, 425–438.
- Park, C.Y., Shcheglovitov, A., and Dolmetsch, R. (2010). The CRAC channel activator STIM1 binds and inhibits L-type voltage-gated calcium channels. *Science* **330**, 101–105.
- Prakriya, M., and Lewis, R.S. (2015). Store-Operated Calcium Channels. *Physiol. Rev.* **95**, 1383–1436.
- Ryu, C., Jang, D.C., Jung, D., Kim, Y.G., Shim, H.G., Ryu, H.H., Lee, Y.S., Linden, D.J., Worley, P.F., and Kim, S.J. (2017). STIM1 Regulates Somatic Ca²⁺ Signals and Intrinsic Firing Properties of Cerebellar Purkinje Neurons. *J. Neurosci.* **37**, 8876–8894.
- Schindelin, J., Arganda-Carreras, I., Frise, E., Kaynig, V., Longair, M., Pietzsch, T., Preibisch, S., Rueden, C., Saalfeld, S., Schmid, B., et al. (2012). Fiji: an open-source platform for biological-image analysis. *Nat. Methods* **9**, 676–682.
- Schwarz, Y., Zhao, N., Kirchhoff, F., and Bruns, D. (2017). Astrocytes control synaptic strength by two distinct v-SNARE-dependent release pathways. *Nat. Neurosci.* **20**, 1529–1539.
- Schwarz, Y., Oleinikov, K., Schindeldecker, B., Wyatt, A., Weißgerber, P., Flockerzi, V., Boehm, U., Freichel, M., and Bruns, D. (2019). TRPC channels regulate Ca²⁺-signaling and short-term plasticity of fast glutamatergic synapses. *PLoS Biol.* **17**, e3000445.
- Sousa, S.R., Vetter, I., Ragnarsson, L., and Lewis, R.J. (2013). Expression and pharmacology of endogenous Cav channels in SH-SY5Y human neuroblastoma cells. *PLoS One* **8**, e59293.
- Stegner, D., Hofmann, S., Schuhmann, M.K., Kraft, P., Herrmann, A.M., Popp, S., Höhn, M., Popp, M., Klaus, V., Post, A., et al. (2019). Loss of Orai2-Mediated Capacitative Ca²⁺ Entry Is Neuroprotective in Acute Ischemic Stroke. *Stroke* **50**, 3238–3245.
- The ENCODE Project Consortium. (2012). An integrated encyclopedia of DNA elements in the human genome. *Nature* **489** (7414), 57–74. <https://doi.org/10.1038/nature11247>.
- Turecek, J., Jackman, S.L., and Regehr, W.G. (2017). Synaptotagmin 7 confers frequency invariance onto specialized depressing synapses. *Nature* **551**, 503–506.
- Wegierski, T., and Kuznicki, J. (2018). Neuronal calcium signaling via store-operated channels in health and disease. *Cell Calcium* **74**, 102–111.
- Wissenbach, U., Philipp, S.E., Gross, S.A., Cavalié, A., and Flockerzi, V. (2007). Primary structure, chromosomal localization and expression in immune cells of the murine ORAI and STIM genes. *Cell Calcium* **42**, 439–446.
- Yuan, J.P., Zeng, W., Dorwart, M.R., Choi, Y.J., Worley, P.F., and Muallem, S. (2009). SOAR and the polybasic STIM1 domains gate and regulate Orai channels. *Nat. Cell Biol.* **11**, 337–343.
- Zheng, S., Zhou, L., Ma, G., Zhang, T., Liu, J., Li, J., Nguyen, N.T., Zhang, X., Li, W., Nwokonko, R., et al. (2018). Calcium store refilling and STIM activation in STIM- and Orai-deficient cell lines. *Pflugers Arch.* **470**, 1555–1567.
- Zhou, Y., Nwokonko, R.M., Cai, X., Loktionova, N.A., Abdulqadir, R., Xin, P., Niemeyer, B.A., Wang, Y., Trebak, M., and Gill, D.L. (2018). Cross-linking of Orai1 channels by STIM proteins. *Proc. Natl. Acad. Sci. USA* **115**, E3398–E3407.
- Zweifach, A., and Lewis, R.S. (1995a). Rapid inactivation of depletion-activated calcium current (ICRAC) due to local calcium feedback. *J. Gen. Physiol.* **105**, 209–226.
- Zweifach, A., and Lewis, R.S. (1995b). Slow calcium-dependent inactivation of depletion-activated calcium current. Store-dependent and -independent mechanisms. *J. Biol. Chem.* **270**, 14445–14451.

STAR★METHODS

KEY RESOURCES TABLE

REAGENT or RESOURCE	SOURCE	IDENTIFIER
Antibodies		
anti STIM1 / GOK antibody mouse monoclonal	Acris Antibodies GmbH	Cat# AM20946PU-N,RRID:AB_10849514
GOK/STIM1 mouse monoclonal, AA 25-139	BD Biosciences	Cat# 610954, RRID:AB_398267
STIM1, Rabbit Polyclonal, AA 2-350	Proteintech	Cat# 11565-1-AP, RRID:AB_2302808
STIM1B	Selfmade, Dr. Martin Jung	This paper
STIM2, Rabbit Polyclonal, 525-674aa encoded by BC146661	Proteintech	Cat# 21192-1-AP, RRID:AB_10734322
Mouse Anti-beta-Actin Monoclonal Antibody, Unconjugated, Clone AC-15	Sigma-Aldrich	Cat# A1978, RRID:AB_476692
Rabbit Anti-GAPDH Monoclonal Antibody, Unconjugated, Clone 14C10	Cell Signaling Technology	Cat# 2118, RRID:AB_561053
mCherry, Polyclonal	Biorbyt	Cat# orb11618, RRID:AB_2687829
RFP/mKate2, Polyclonal	Evrogen	Cat# AB233, RRID:AB_2571743
Anti-Bassoon, mouse monoclonal	Synaptic Systems	Cat# 141 011, RRID:AB_2619827
Goat anti-Mouse IgG Alexa Fluor 555	Invitrogen	Cat #A-21422
Goat anti-Rabbit IgG Alexa Fluor 488	Invitrogen	Cat #A32731
Goat anti-Guinea Pig IgG Alexa Fluor 643	Invitrogen	Cat #A-21450
Chemicals, peptides, and recombinant proteins		
GIBCO's Minimum Essential Medium (MEM)	Thermo Fisher Scientific	Cat #31095029
GIBCO's Dulbecco's modified eagle's medium (DMEM)	Thermo Fisher Scientific	Cat #41966029
GIBCO's Fetal Calf serum (FCS)	Thermo Fisher Scientific	Cat #10270106
GIBCO's Non-Essential amino acids (NEAA)	Thermo Fisher Scientific	Cat #11140050
GIBCO's Phosphate buffered Saline (PBS), pH 7.4	ThermoFisher Scientific	Cat #10010023
TriZOL	Life technologies	Cat #15596026
cOmplete Protease Inhibitor Cocktail	Roche	Cat #4693159001
Neurobasal A Medium	ThermoFisher Scientific	Cat #10888022
B-27 Supplement	ThermoFisher Scientific	Cat #17504044
GIBCO's GlutaMAX	ThermoFisher Scientific	Cat #35050061
Papain	Worthington Biochemical	Cat #LS003126
GIBCO's Penicillin/Streptomycin	ThermoFisher Scientific	Cat #15140122
poly-D-lysine	Sigma-Aldrich	Cat #P6407
Critical commercial assays		
JetPRIME	Polyplus	Cat #114-15
JetOptimus	Polyplus	Cat #117-07
DreamTaq Green PCR master mix	Thermo Fisher Scientific	Cat #K1081
SuperScriptTMII Reverse Transcriptase	Thermo Fisher Scientific	Cat # 18064022
Quantitect SYBR green	QIAGEN	Cat #204143
Clarity Western ECL blotting substrate	Bio-Rad	Cat #1705061
Pierce BCA Protein Assay Kit	ThermoFisher Scientific	Cat #23227
Lipofectamine 2000	Invitrogen	Cat #11668027
Dynabeads Protein A for Immunoprecipitation	ThermoFisher Scientific	Cat #10001D
Dynabeads Protein G for Immunoprecipitation	ThermoFisher Scientific	Cat #10003D
ProLong Gold Antifade Mountant with DAPI	ThermoFisher Scientific	Cat # P36931
Nitrocellulose membranes	GE Healthcare Lifesciences	Cat #10600016
Zombie Aqua	Biolegend	Cat # 423101

(Continued on next page)

Continued		
REAGENT or RESOURCE	SOURCE	IDENTIFIER
Gateway BP Clonase II Enzyme mix	ThermoFisher Scientific	Cat #11789020
Gateway LR Clonase II Enzyme mix	ThermoFisher Scientific	Cat #11791020
Experimental models: cell lines		
HEK STIM1 ^{-/-} ;STIM2 ^{-/-} (S1/S2 DKO)	kind gift by Dr. Don Gill	N/A
HEK Orai1 ^{-/-} ; Orai2 ^{-/-} ; Orai3 ^{-/-} (Orai TKO)	Alansary et al., 2020	N/A
MEF STIM1 ^{-/-} ;STIM2 ^{-/-} (S1/S2 DKO)	Oh-Hora et al., 2008	N/A
SH-SY5Y STIM1 ^{-/-} ;STIM2 ^{-/-} (S1/S2 DKO)	this study	N/A
SH-SY5Y STIM1 ^{-/-} (S1 KO)	this study	N/A
Experimental models: organisms/strains		
C56Bl/6N	Charles River	Strain code 027
Oligonucleotides		
See Table S1 for oligonucleotide information.		N/A
Recombinant DNA		
Plasmid: pX459-pSpCas9(BB)-2A-Puro V2.0	Addgene	#62988
Plasmid: pWPXL	Addgene	#12257
Plasmid: pEX-SP-YFP-STIM1	Addgene	#18857
Plasmid: pEX-SP-YFP-STIM1B	this study	N/A
Plasmid: pEX-SP-YFP-STIM1_514*	this study	N/A
Plasmid: pMax-mCherry-STIM1	Kilch et al., 2013	N/A
Plasmid: pEX-S1SP-mKate2-STIM2	this study	N/A
Plasmid: pMax-Stim1-IRES-mCherry	this study	N/A
Plasmid: pMax-Stim1B-IRES-mCherry	this study	N/A
Plasmid: pMax-Stim1_514*-IRES-mCherry	this study	N/A
Plasmid: pMax-Stim1B ØSTOP- IRES-mCherry	this study	N/A
Plasmid: pMax-Orai1-IRES-GFP	Wissenbach et al., 2007	N/A
Plasmid: pMax-Orai2-IRES-GFP	Wissenbach et al., 2007	N/A
Plasmid: pCAGGS-Orai3-IRES-GFP	Wissenbach et al., 2007	N/A
Plasmid: pMax-mKate2-Stim1	this study	N/A
Plasmid: pMax-mKate2-Stim1B	this study	N/A
Plasmid: pMax-mKate2-Stim1BØSTOP	this study	N/A
Plasmid: pMax-mKate2-Stim1B L373S/A376S	this study	N/A
Plasmid: pWPXL-mKate2-Stim1	this study	N/A
Plasmid: pWPXL-mKate2-Stim1B	this study	N/A
Plasmid: pWPXL-mKate2-Stim1BØSTOP	this study	N/A
Plasmid: pWPXL-mKate2-Stim1B L373S/A376S	this study	N/A
Plasmid: PLCδ-PH-mCherry	Kind gift by Dr. Nicolas Touret	N/A
Plasmid: pmaxGFP	Lonza	N/A
Plasmid: pBabe-CMV-YFP _N -DEST-neo34	Kind gift by Dr. Yubin Zhou	N/A
Plasmid: pBabe-CMV-YFP _C -DEST-puro	Kind gift by Dr. Yubin Zhou	N/A
Plasmid: pDONR221-STIM1	Kind gift by Dr. Yubin Zhou	DNAsu #76162
Plasmid: pDONR221-STIM2	DNAsu Repository	DNAsu #746184
Plasmid: pBabe-STIM2-YFP _N	this study	N/A
Plasmid: pMax-STIM1-YFP _C	this study	N/A
Plasmid: pMax-STIM1B-YFP _C	this study	N/A
Software and algorithms		
Quantity One	Bio-Rad	
Fiji	Schindelin et al., 2012	

(Continued on next page)

Continued

REAGENT or RESOURCE	SOURCE	IDENTIFIER
Patchmaster/ Pulse	HEKA Elektronik	
Prism 8.4	GraphPad	
Igor Pro 6.37	WaveMetrics	
Python scripts for Ca ²⁺ imaging analysis	https://github.com/lukasjarzembowski/Fura2-Calcium-Analysis	
SigmaPlot 13	Systat Software GmbH	
FACSVerse system	BD Biosciences	
FloJo 10.0.7	BD Biosciences	
VisiView®	Visitron Systems GmbH	
Mini Analysis, Version 6.0.3	Synaptosoft Inc.	

RESOURCE AVAILABILITY

Lead contact

All requests for resources and reagents should be directed to the lead contact, Dr. Barbara A. Niemeyer (barbara.niemeyer@uks.eu).

Materials availability

Constructs and cell lines available upon request, MTA required for cell lines.

Data and code availability

Custom-written Python routines are available at <https://github.com/lukasjarzembowski/Fura2-Calcium-Analysis>.

EXPERIMENTAL MODEL AND SUBJECT DETAILS

Animals

All experimental procedures involving the use of animals were approved and performed in accordance with EU guidelines and the ethic regulations of the animal welfare committee at the University of Saarland. All efforts were made to minimize animal suffering and to reduce the number of animals used. Autaptic cultures of hippocampal neurons were prepared from P0-1 wild-type (C56Bl/6N strain) mice of both sexes as described previously ([Schwarz et al., 2017](#)).

Cell culture of cell lines

All cell lines were maintained in a humidified incubator at 37°C, 5% CO₂ and passaged weekly. HEK293 Orai1^{-/-};Orai2^{-/-};Orai3^{-/-} cells were cultured in Minimum Essential Medium (MEM, GIBCO). Dulbecco's modified eagle's medium (DMEM, GIBCO) was used for HEK STIM1^{-/-};STIM2^{-/-} and MEF Stim1^{-/-};Stim2^{-/-}. SH-SY5Y STIM1^{-/-} and SH-SY5Y STIM1^{-/-};STIM2^{-/-} cells were maintained in DMEM with 1% non-essential amino acids (NEAA, GIBCO). All media was supplemented with 10% fetal calf serum (FCS, ThermoFisher Scientific).

Primary hippocampal neuron cultures

Briefly, hippocampi were dissected and digested for 28 mins at 37°C with 15 units of papain (Worthington, USA), followed by gentle mechanical trituration. Neurons were seeded at low density (1.000 cells/ml) onto a layer of glial microislands, resulting in co-cultures of glia and neurons. For electrophysiological recordings, only islands with single neurons were used. For mass cultures, neurons were seeded with a density of 300 cells/mm² on 25 mm coverslips coated with 0.5 mg/ml of poly-D-lysine (Sigma). Cultures were maintained at 37°C in an incubator, humidified with 95% air and 5% CO₂ in NBA (Invitrogen), supplemented with 2% B-27 (Sigma), 1% GlutaMAX (Invitrogen), and 1% penicillin/streptomycin (Invitrogen).

Generation of CRISPR-Cas9-mediated STIM1/STIM2 knockout cell lines

Sequence-specific gRNA for STIM1 and STIM2 as described in [Zhou et al. \(2018\)](#) were subcloned into pX459-pSpCas9(BB)-2A-Puro V2.0 using the BbsI recognition site. Single or double transfections of the CRISPR plasmids or control plasmids into SH-SY5Y cells were performed using Lipofectamin2000 according to manufacturer's instructions. Cells were selected in media containing 2 μg/μl puromycin. Monoclonal cell lines were generated by limiting dilution and knockout was verified by sequencing genomic DNA, by western blot for STIM1 and STIM2 and by intracellular Ca²⁺ measurements ([Figures 2A](#)).

METHOD DETAILS

Plasmids and cloning

A detailed listing of all constructs used in this study can be found in the [Key resources table](#). Murine and human STIM1B constructs were created by insertion of the 36bp Exon B specific nucleotides via PCR into pEX-SP-YFP-STIM1 (Liou et al., 2005; Addgene #18857) and pMax-Stim1-IRES-mCherry vectors using phosphorylated primer pairs. STIM1₅₁₄ constructs were created by QC PCR insertion of two subsequent stop codons into Stim1 (pMax-IRES-mCherry) and STIM1 (pEX) vectors using primers 1498/99 (human) or by PCR amplification and restriction site cloning with primer 1566 for murine variant. mKate2-tagged Stim1 variants were cloned via amplification of mKate2 from pmKate2-N (Evrogen) with phosphorylated 1719/20 primer pairs and subsequent blunt ligation after the signal peptide of amplified and linearized pMax-Stim1 using 1604/05 primer pairs. This construct was used for creation of mKate2-Stim1B using the insertion PCR strategy described above and subsequent mutation of the CAD domain (Stim1B L373S,A376S) or deletion of the Exon B stop codon (Stim1B Δ Stop) via site-directed mutagenesis using 1796/97 or 1794/95 primer pairs, respectively. Murine mKate2-tagged Stim1 constructs were amplified with BamHI and SpeI sites using 1744/45 primer pairs and subcloned into the lentiviral expression vector pWPXL (Addgene #12257) replacing the EGFP cassette. Murine Orai variants in pCAGGS-IRES-GFP were described previously (Wissenbach et al., 2007). BIFC destination constructs pBabe-CMV-YFP_N-DEST-neo34, pBabe-CMV-YFP_C-DEST-puro containing split-YFP and pDONR221-STIM1 entry clone (DNAsu #76162) were a kind gift by Dr. Yubin Zhou. STIM2 entry clone in pDONR221 donor plasmid (#746184) were purchased from the DNAsu repository. pDONR221-STIM1B entry clone was created by amplification of STIM1B with *attB*-sites using primers 1909/1931 from pMax-STIM1B-IRES-mCherry and using the Gateway BP Clonase II Enzyme mix (ThermoFisher Scientific). pBabe-STIM1-YFP_C, pBabe-STIM1B-YFP_C and pBabe-STIM2-YFP_N were created from entry clones using Gateway LR Clonase II Kit (ThermoFisher Scientific). pMax-STIM1-YFP_C was cloned by amplification with DraIII and PaeR71 sites using primers 704/1996 from pBabe-STIM1-YFP_C (not used in this study), replacing c-terminal STIM1 residues and mCherry tag in pMax-STIM1-mCherry. pMax-STIM1B-YFP_C was created by replacing the STIM1 coding sequence with STIM1B from pBabe-STIM1B-YFP_N (not used in this study) using BamHI and BspHI sites. All constructs were verified by sequencing (Microsynth Seqlab, Göttingen). All primers were synthesized by Eurofins Genomics (Ebersberg, Germany).

Transfection

For electrophysiology and TIRF experiments, HEK cells were electroporated with 2 μ g of plasmid DNA in Opti-MEM (GIBCO) medium using a Nucleofector 2b device (Lonza). Lentiviral particles were produced in HEK293T cells as previously described (Schwarz et al., 2017). Primary neurons were transfected with 5 to 10 μ L of viral suspension at 1-3DPC. For all Ca²⁺ imaging and widefield imaging experiments, jetPRIME (Polyplus) reagent was used according to the manufacturer's instructions. For BIFC experiments, HEK cells were transfected using jetOPTIMUS (Polyplus).

PCR and quantitative real-time PCR

To synthesize cDNA, cells or tissues were harvested in TRIzol (Life technologies) and RNA was isolated according to the manufacturer's instructions. RNA was then transcribed to cDNA using SuperScriptTMIII Reverse Transcriptase (Life technologies). For the analytic PCR, DreamTaq Green PCR Master Mix (Thermo Fisher Scientific) was used. Amplified PCR products were separated on GTQ-agarose gels and visualized with peqGREEN DNA stain (VWR) on a ChemiDoc XRS+ system (Bio-Rad). qRT-PCR was performed using QuantiTect SYBR green kit (QIAGEN) and a CFX96 qPCR system (Bio-Rad) with primers listed in [Key resources table](#). For quantification, expression levels are presented as the normalized quantification cycle (Cq) values of the gene of interest to that of TBP (TATA box-binding protein, M.m.) and HPRT1 (M.m) or to TBP (H.s.) and RNA Pol (H.s.) using the DCT method (relative differences were comparable when normalized to RNA polymerase). Values are shown as 2^{- Δ Cq} or as relative amounts.

Biochemistry

Mice brain tissue was washed with PBS and homogenized with a 22 gauge needle 18 times in ice cold lysis buffer (20mM Tris, pH 7.4, 100mM KCl, 10% glycerol (v/v), 1% n-dodecyl β -D-maltoside (DDM)) supplemented with cOmplete protease inhibitor (Roche). Transfected cells were washed with PBS, detached with a cell scraper and re-suspended in ice cold lysis buffer. Tissue and cell lysates were subsequently centrifuged for 20 min at 18000 rpm and 4°C. The protein concentration of the supernatant was determined using Pierce BCA Protein Assay Kit (ThermoFisher). 50-75 μ g total protein was denatured at 65°C for 15 minutes in Laemmli loading buffer. Immunoprecipitations were performed by incubating antibodies against Stim1 (see [Key resources table](#)) with Dynabeads Protein A/G (ThermoFisher Scientific) for 2 hours at 4°C, followed by adding the pre-cleared protein lysates to it and incubated overnight at 4°C. The beads were washed 4 times with ice-cold lysis buffer before being eluted with 2X laemmli loading dye. Eluted protein fractions were denatured at 65°C for 15 minutes. Discontinuous SDS-PAGE was performed with subsequent electrotransfer to nitrocellulose membranes (GE Healthcare) for 90 minutes at 150mA and 4°C. Membranes were blocked with 5% skimmed-milk in TBS-T buffer for 60 minutes. Membranes were incubated with primary antibodies (see [Key resources table](#)) diluted in 3% BSA in TBS buffer overnight at 4°C. Membranes were washed three times with TBS-T and incubated for 90 minutes with horseradish peroxidase-coupled secondary antibodies in blocking buffer at room temperature. After three washing steps in TBS-T and TBS, membranes were incubated in Clarity Western ECL Substrate (Bio-Rad) for 5 minutes and detection of chemiluminescence was performed on

a CCD camera equipped ChemiDoc XRS+ system (Bio-Rad). Densitometric quantification of non-saturated signals was done using Quantity One software (Bio-Rad).

Electrophysiological measurements of I_{CRAC}

Recordings of I_{CRAC} were performed in the whole-cell voltage clamp configuration at room temperature as previously described (Kilch et al., 2013). Briefly, HEK $STIM1^{-/-};STIM2^{-/-}$ cells were co-transfected with Stim1 or Stim1b IRES-mCherry and Orai1-3 IRES-GFP plasmids at a 3:1 ratio and recordings were obtained 24 hours post-transfection with an EPC-10 patch-clamp amplifier controlled by Patchmaster software (HEKA Electronics). Series resistance was compensated to 85%. All voltages were corrected for a liquid junction potential of 10 mV. Currents were filtered at 2.9 kHz (four-pole Bessel filter) and digitized at 10 kHz. After establishment of whole-cell configuration, linear voltage ramps from -150 mV to $+150$ mV (50 ms duration) were applied every 2 s from a holding potential of 0 mV for 300 s. Pipette solution contained the following (in mM): 120 Cs glutamate/140 Cs Aspartate, 3 $MgCl_2$, 20 Cs-BAPTA / 2 EGTA, 10 HEPES and 0.05 IP_3 (pH 7.2 with CsOH, 298 mOsm). Bath solution contained (in mM): 120 NaCl, 10 TEA-Cl, 10 $CaCl_2$, 2 $MgCl_2$, 10 HEPES and glucose (pH 7.2 with NaOH). For analysis of I_{CRAC} , currents were analyzed at -130 mV and for 300 s after break-in using IgorPro 6.37 (Wavemetrics). The data was then imported into GraphPad 8.4 (Prism) for further statistical analysis and plotting.

Recordings of autaptic synaptic currents

Synaptic currents were recorded at room temperature in the whole-cell voltage clamp mode from autaptic neurons after 9–15 days of culture. Patch pipettes (R_{tip} 4–5.5 M Ω) were filled with the following intracellular solution (in mM): 137.5 K-gluconate, 11 NaCl, 2 MgATP, 0.2 Na_2GTP , 1.1 EGTA, 11 HEPES, 11 D-glucose, pH 7.3 with KOH and extracellular solution containing (in mM) 130 NaCl, 10 $NaHCO_3$, 2.4 KCl, 1–2 $CaCl_2$, 2 $MgCl_2$, 10 HEPES, 10 D-glucose, pH 7.3 with NaOH, osmolarity 290 mOsm was used. To prevent synaptic plasticity changes NMDA-receptor blocker D-2-amino-5-phosphonopentanoate (APV; 50 μ M) was added. The reversal potential of chloride-mediated currents was adjusted to the holding potential to avoid the potential contribution of GABAergic currents. Exemplary neurons were treated with 25 μ M DNQX (data not shown) to confirm the recordings of AMPA receptor (AMPA) currents. Neurons were voltage-clamped at -70 mV with an EPC10 amplifier (HEKA Electronic) under control of Pulse 8.5 program (HEKA Electronic) and stimulated by membrane depolarizations to $+10$ mV for 0.7 ms every 5 s (0.2 Hz). Cells with an average access resistance of 6–15 M Ω , with 75%–80% resistance compensation and < 100 pA leak-current were analyzed. Current signals were low-pass filtered at 2.9 kHz (four pole Bessel filter EPSC10) and digitized at a rate of 10 or 50 kHz. Miniature EPSCs were analyzed using a commercial software (Mini Analysis, Synaptosoft, Version 6.0.3). To determine mEPSC properties with reasonable fidelity and to prevent the detection of “false events” (due to random noise fluctuations), only spontaneous mEPSCs with a peak amplitude exceeding > 5 times the standard deviation of the baseline noise and a charge criterion > 25 fC were considered. The AP-evoked EPSC amplitude and charge were determined from the average of 10 EPSCs recorded at 0.2 Hz. The RRP size during HFS was quantified from the cumulative synchronous EPSC charge integral during the 20 Hz train. For this, the total charge of each action potential evoked response within the train was corrected by subtracting the integral of the steady state current component (= asynchronous charge) determined at the end of the stimulus interval. The cumulative plot of the resulting synchronous release component reports the decrement in RRP size followed by a sustained phase of charge increase reflecting the steady-state phase of ongoing RRP vesicle replenishment. The sustained phase of secretion (last 5 data points) was approximated by linear regression. When back-extrapolated to time 0, its y-intercept provides an estimate of the RRP size with minimal contribution of refilling.

TIRF and widefield microscopy of cluster formation

Cluster formation of STIM1 and STIM1B was monitored using a Leica AM TIRF MC system. HEK $STIM1^{-/-};STIM2^{-/-}$ cells were electroporated with 0.5 μ g of the PIP2 sensor PLC δ -PH-mCherry and either 1.5 μ g of YFP-hSTIM1 or YFP-hSTIM1B and seeded on 25-mm glass coverslips. 24h after transfections the coverslips were transferred to a self-built perfusion chamber and washed with 0.5 mM Ca^{2+} ringer. Images were taken with a 100x1.47 oil HCX PlanApo objective and YFP and mCherry were excited using 488nm or 561 nm lasers with BP525/50 and BP600/40 emission filters, respectively. The TIRF focal plane was set according to the PLC δ -PH-mCherry signal and a penetration depth of 200nm was chosen. 1–2 cells in the field of view were imaged at 0.2 Hz for 10 minutes with equal intensity, exposure and gain settings between groups per day. Store-depletion and subsequent cluster formation was induced after 60 s baseline acquisition via perfusion of 1ml 0.5 mM Ca^{2+} ringer containing 1 μ M Thapsigargin at room temperature.

Widefield images of HEK293 $Orai1^{-/-};Orai2^{-/-};Orai3$ cells were taken on an Zeiss Axio Observer 7 inverted microscope equipped with a Prime95B sCMOS camera (Photometrics) using a Zeiss 63x/1.40 Plan-Apochromat oil objective. YFP and mCherry signals were excited using a HXP 120 V compact light source with 480–498nm/560–584nm excitation filters and Fura8 (BS488nm, BP500–550nm)/63 HE Red (BP559–585nm, BS590nm, BP600–690nm) emission filter cubes. Cells were imaged in a Z-plane near the plasma membrane set according to the PLC δ -PH-mCherry signal before and 10 minutes after addition of 1 μ M Thapsigargin in 0.5 mM Ca^{2+} ringer.

Fura2-based Ca^{2+} Imaging

MEF $Stim1^{-/-};Stim2^{-/-}$ cells were seeded on 25mm coverslips 24 hours before transfection with 2 μ g of mKate, mKate2-Stim1 mKate2-Stim1B or mKate2-mStim1B Δ STOP (all pMax). SH-SY5Y $STIM1^{-/-};STIM2^{-/-}$ or SH-SY5Y $STIM1^{-/-}$ cells were seeded

in 35mm cell culture dishes 24 hours before transfection with 1 μ g of either YFP-STIM1, YFP-STIM1B or YFP-STIM1_514* (all pEX) with 1 μ g mKate (pMax). Transfected SH-SY5Y STIM1^{-/-};STIM2^{-/-} or SH-SY5Y STIM1^{-/-} cells were reseeded 4 hours post transfection on 25mm coverslips. After 16-24hours, cells were loaded with 1 μ M Fura2-AM in DMEM + 10%FCS (+ 1% NEAA for SH-SY5Y cells) for 30min at RT and transferred to a self-built, high exchange rate and low volume perfusion chamber and washed with external Ca²⁺ Ringer solution containing (in mM): 155 NaCl, 2 MgCl₂, 10 glucose, 5 HEPES and 0.5-1.5 CaCl₂ (0.5-2 Ca²⁺ Ringer) or no CaCl₂, but 1 EGTA and 3 MgCl₂ instead (0 Ca²⁺ Ringer, pH 7.4 with NaOH). High K⁺ ringer was prepared by equimolar substitution of NaCl with 100 mM KCl in 1.5 mM Ca²⁺. ER stores were depleted with 1 μ M Thapsigargin (Tg) in 0 mM Ca²⁺ (readdition protocol) or 1.5 mM Ca²⁺ (global protocol) ringer solution. The imaging setup consisted of a Zeiss Axio Observer A1 inverse microscope, Polychrome V (TILL Photonics) light source and Clara CCD camera (Andor). F76-521 Fura-2 HC, F36-528 YFP and F20-451 RFP filter cubes (AHF Analysetechnik AG) were used. 340nm and 380nm images were acquired at 0.2 Hz with 20ms-30ms exposure time and 1x1 (SH-SY5Y cells) or 2x2 (MEF cells) pixel binning through 10x0.50 Fluor or 20x0.75 Fluor (Zeiss) objectives. Acquisition was controlled by and background-subtracted 340/380nm ratio values were calculated using VisiView® Software. Ratio data was further analyzed and filtered using IgorPro (Wavemetrics) or custom-written Python routines (available at <https://github.com/lukasjarzembowski/Fura2-Calcium-Analysis>) in JupyterLab. For kinetic parameters, average (5-10 frames) basal and plateau ratio values and maximal Tg-, Ca²⁺-readdition- or High K⁺-induced peak ratio values were determined. To obtain Δ s, the average ratio (5-10 frames) before addition of Tg, Ca²⁺ or High K⁺ ringer was subtracted, respectively. The influx rate is represented by the slope of a linear fit performed on the ratio values of 1 frame before and 4 frames after Ca²⁺ readdition. For quantification of global Ca²⁺ entry, the area under curve upon store-depletion was determined. The data was then imported into GraphPad 8.4 (Prism) for further statistical analysis and plotting.

Bimolecular fluorescence complementation

1.2x 10⁵ HEK STIM1^{-/-};STIM2^{-/-} cells were seeded in 6 well plates and transfected with a total amount of 2 μ g DNA. STIM1 or STIM1B fused with AA 156-720 of YFP (pMax STIM1(B)-YFP_C) were used as baits. STIM2 and a negative control fused to AA1-155 of YFP (pBabe STIM2-YFP_N) served as prey. Transfection was performed at equimolar ratios of DNA. 24h post transfection 1 μ M Thapsigargin (Tg) was added to the media and incubated for 10 min to induce SOCE. After incubation cells were washed once and detached in PBS containing 1 μ M Tg. Cells were centrifuged at 320 g in FACS tubes at 4°C for 10 min and resuspended in 400 μ l ice cold FACS buffer (5% FCS, 0.5% BSA 0.07% NaN₃ in PBS) with additional Zombie Aqua (1:1000 Fixable Viability Kit, BioLegend) to stain for vital cells. A FACSVerser system (BD Biosciences) was used to screen for YFP signal in vital cells. Analysis was done using BD FACSuite as well as FloJo 10.0.7 (BD Biosciences), calculating the percentages of YFP positive cells (Jing et al., 2015).

Immunostaining

MEF Stim1^{-/-};Stim2^{-/-} cells co-expressing Stim1 and Stim1B were fixed with 3% PFA for 15 min at RT. After washing with 0.25 mM Ca²⁺ Ringer, cells were permeabilized with 0.1% Triton for 5-10 min. Unspecific epitopes were blocked using 4% BSA in PBS for 30 min RT. Primary and secondary antibodies were diluted in blocking solution and incubated over night at 4°C (primary antibody) and for 30 min at room temperature (secondary antibody). Cells and tissue sections were mounted with ProLong Gold Antifade Mountant with DAPI (Thermo Fisher Scientific). Primary and secondary antibodies used for immunocytochemistry are listed in the [Key resources table](#). Images were acquired as z stacks on a confocal microscope LSM 700 (Zeiss) with a \times 63/1.4 NA oil objective. Mass hippocampal neurons were fixed for 10 min (RT) in PBS containing 4% paraformaldehyde. Cells were quenched for 10 min with 50mM NH₄Cl in PBS, blocked for 30 min in PBS containing 3% BSA and 0.1% Triton X-100. Primary (anti-bassoon, 1:500, Synaptic Systems; anti-RFP, 1:500 and secondary antibodies (1:1000, Alexa Fluor 555, Alexa Fluor 488 and Alexa Fluor 643-conjugated goat anti-mouse or goat anti-rabbit; Invitrogen) were diluted in blocking buffer. Primary antibodies were incubated and secondary antibodies for 1.5h at RT, respectively. Neurons were imaged either on a confocal microscope (LSM 710; Zeiss) using AxioVision 2008 software (Carl Zeiss) or an Axiovert200 (Zeiss), fluorescence was elicited with a Polychrome V monochromator (Till Photonics) and captured with a EMCCD camera (Evolve, Visitron, Germany).

QUANTIFICATION AND STATISTICAL ANALYSIS

Quantification of colocalization

Confocal images of MEF cells were processed using Fiji and are presented as Maximum Intensity Projections (MIPs). Manders' coefficients of background-subtracted images were determined using Fiji's built-in Coloc2 plug-in.

Quantification of TIRF microscopy data

TIRF images were analyzed using Fiji (Schindelin et al., 2012) and converted to 32-bit. The background was removed using rolling ball background subtraction with the radius set to the approximate diameter of the largest cluster at 10 minutes (median STIM1: 15, STIM1B, 12 pixels). Two times the standard deviation of the mean fluorescence of the cell's footprint at time point 0 was chosen as lower threshold and pixels below that set to NaN. The YFP integrated density in a ROI covering the footprint of the cell was determined for each time point and resulting values imported into GraphPad 8.4 (Prism) for further (statistical) analysis. The signals were normalized (F/F₀) and a linear fit to calculate the rate of cluster formation was performed on the linear portion after onset of cluster

formation. Before the size of clusters was determined, Fiji's watershed algorithm was applied to binary images at $t = 10$ minutes. The "Analyze Particles" tool of Fiji with the size and circularity set to 0.01-5.00 μm and 0.1-1.00, respectively, was used to determine the area of clusters. The data was imported into GraphPad 8.4 (Prism) for further statistical analysis and plotting.

Statistical analysis

No statistical methods were used to predetermine sample sizes. Data collection and analyses were not performed blind to the experimental condition, nor was a method of randomization applied. Statistical analysis was performed using GraphPad 8.4 (Prism) and SigmaPlot 13 (Systat Software GmbH). A significance level of $\alpha = 0.05$ was chosen with * $p < 0.05$, ** $p < 0.01$, *** $p < 0.001$. Gaussian distribution of data was tested using Shapiro-Wilk test. For datasets consisting of two groups, Student's t test with Welch's correction for normal distributed values or Mann-Whitney for non-Gaussian distributed values were used. Kolmogorov-Smirnov test was used for comparing distributions of cluster sizes. For comparison of more than two groups, one-way ANOVA on ranks or Kruskal-Wallis was used followed by Dunn's post hoc test. Descriptive statistics of data, numbers of cells, technical and biological replicates are described in figure legends. In all cases, results were obtained from ≥ 3 biological replicates with each 2-8 technical replicates.